ARTICLES
https://doi.org/10.1038/s41557-021-00666-6

nature chemistry

Magnetic ordering through itinerant ferromagnetism in a metal–organic framework

Jesse G. Park[1], Brianna A. Collins[2], Lucy E. Darago[1], Tomče Runčevski[3], Michael E. Ziebel[1], Michael L. Aubrey[1], Henry Z. H. Jiang[1,4], Ever Velasquez[5], Mark A. Green[6], Jason D. Goodpaster[2] and Jeffrey R. Long[1,4,5] ✉

Materials that combine magnetic order with other desirable physical attributes could find transformative applications in spintronics, quantum sensing, low-density magnets and gas separations. Among potential multifunctional magnetic materials, metal–organic frameworks, in particular, bear structures that offer intrinsic porosity, vast chemical and structural programmability, and the tunability of electronic properties. Nevertheless, magnetic order within metal–organic frameworks has generally been limited to low temperatures, owing largely to challenges in creating a strong magnetic exchange. Here we employ the phenomenon of itinerant ferromagnetism to realize magnetic ordering at $T_c = 225$ K in a mixed-valence chromium(II/III) triazolate compound, which represents the highest ferromagnetic ordering temperature yet observed in a metal–organic framework. The itinerant ferromagnetism proceeds through a double-exchange mechanism, which results in a barrierless charge transport below the Curie temperature and a large negative magnetoresistance of 23% at 5 K. These observations suggest applications for double-exchange-based coordination solids in the emergent fields of magnetoelectrics and spintronics.

The development of multifunctional magnets with optimized magnetic properties in concert with other physical properties, such as porosity and high magnetoresistance, remains a daunting challenge, but with the promise to enable new applications in green technologies[1] and next-generation data processing and storage[2,3]. For the realization of commercial applications, it is crucial for a magnet to exhibit a high magnetic ordering temperature beyond potentially elevated operating temperatures. The vast majority of solid-state permanent magnets with high ordering temperatures are based on itinerant magnetism[4]. In particular, a specific form of itinerant magnetism, known as a double-exchange mechanism, was discovered by Zener in 1951 to explain the coexistence of metallic conductivity and high-temperature ferromagnetism in perovskite mixed-valence manganites, which contain Mn^{III} and Mn^{IV} ions connected by bridging O^{2-} ions[5]. Here an itinerant electron is delocalized between the e_g orbitals of neighbouring Mn ions and consequently promotes a parallel alignment of spins for the localized electrons in t_{2g} orbitals, in accordance with Hund's rules. Many such double-exchange solid-state materials, which include cobaltites and Heusler alloys, have since been discovered and investigated for applications in spintronics devices[2,6,7].

As an alternative to traditional solid-state materials, metal–organic frameworks, a subclass of coordination solids, are composed of inorganic building units connected by polytopic organic linkers. Compared with solid-state materials, metal–organic frameworks can offer tremendous synthetic versatility to fine-tune their chemical and physical properties. For instance, organic linkers with predictable binding modes can be utilized to yield frameworks with unique crystal structures and physical properties, which are easily modified through methods such as the substitution of electron donating and/or withdrawing substituents on the ligand, postsynthetic redox chemistry and metal or linker exchange[8–10]. Furthermore, a combination of a long-range magnetic order and porosity in framework materials could lead to the realization of lightweight permanent magnets and magnetic separation media[11–13]. Nevertheless, the overwhelming majority of framework materials are not permanent magnets, owing primarily to the inability of diamagnetic organic linkers to mediate the strong magnetic coupling requisite for long-range order. Indeed, only a few strategies have been developed to synthesize coordination solids with high magnetic ordering temperatures, which include the employment of short diamagnetic inorganic ligands or organic radical ligands, as exemplified by Prussian blue analogues and the amorphous material V(tetracyanoethylene)$_{\sim 2}$, respectively[11,12,14–18]. Alternatively, a potentially powerful, yet unrealized strategy, involves the utilization of itinerant charge carriers via a double-exchange mechanism. In addition to achieving high ordering temperatures in metal–organic magnets that contain diamagnetic linkers, this approach may further provide a means to introduce metallic electronic conductivity.

Although double exchange is a recognized phenomenon in solid-state materials[5–7], examples in coordination solids with organic ligands are limited to molecular compounds[19,20]. Azolate ligands have strong σ-donating and π-accepting abilities, and when coordinated to octahedral metal ions with diffuse d_π orbitals of favourable energies, strong π–d conjugation between the ligand and metal orbitals may arise[19–21]. Furthermore, compact, symmetrical azolate ligands can support crystal structures that consist of infinite metal–azolate chains with short metal–metal distances and an octahedral coordination environment around the metal ions[22], which provides efficient pathways for long-range charge transport and magnetic interaction[23–25]. Here we report the mixed-valence framework material $Cr(tri)_2(CF_3SO_3)_{0.33}$, which exhibits itinerant

[1]Department of Chemistry, University of California, Berkeley, CA, USA. [2]Department of Chemistry, University of Minnesota—Twin Cities, Minneapolis, MN, USA. [3]Department of Chemistry, Southern Methodist University, TX, USA. [4]Materials Sciences Division, Lawrence Berkeley National Laboratory, Berkeley, CA, USA. [5]Department of Chemical and Biomolecular Engineering, University of California, Berkeley, CA, USA. [6]School of Physical Sciences, University of Kent, Canterbury, UK. ✉e-mail: jrlong@berkeley.edu

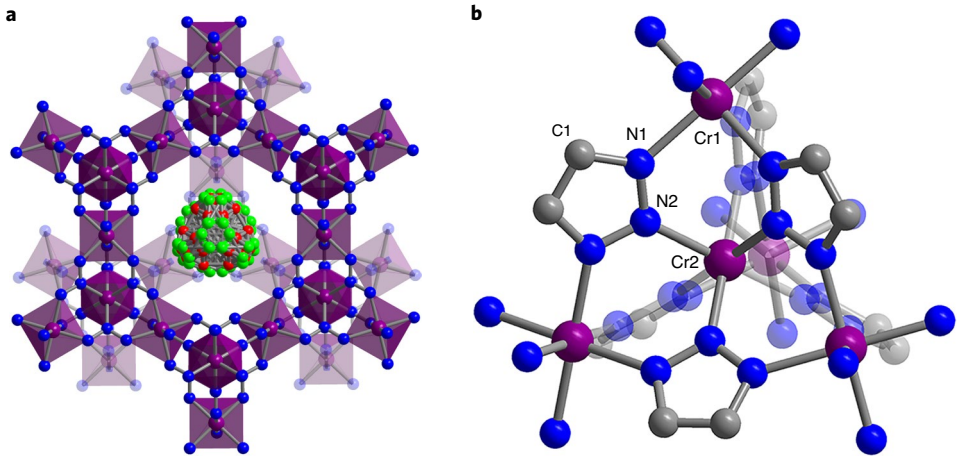

Fig. 1 | Solid-state structures. a, Portions of the Cr–N sublattice of the $Cr(tri)_2(CF_3SO_3)_{0.33}$ structure determined from analysis of powder X-ray diffraction data collected at 360 K, which shows continuous chromium–triazolate chains that form a diamondoid-type lattice and a disordered, charge-balancing trifluoromethanesulfonate anion in the pore cavity. **b**, A tetrahedral, pentanuclear repeating unit. Cr, purple; S, yellow; F, green; O, red; N, blue; C, grey; H atoms are omitted for clarity.

ferromagnetism with a Curie temperature (T_C) of 225 K via a double-exchange mechanism.

Results and discussion

Synthesis and spectroscopic properties. The compound $Cr(tri)_2(CF_3SO_3)_{0.33}$ (Htri, 1*H*-1,2,3-triazole) is formed through a solvothermal reaction between anhydrous $Cr(CF_3SO_3)_2$ and 1*H*-1,2,3-triazole in *N*,*N*-dimethylformamide (Methods and Supplementary Information). The resulting purple solid consists of octahedron-shaped crystals with an edge dimension of ~0.5 µm (Extended Data Fig. 1) and is structurally analogous to reported $M(tri)_2$ (M = Mg, Mn, Fe, Co, Cu, Zn and Cd) materials[24,26,27]. The material has a diamondoid-type structure formed by corner-sharing tetrahedral pentanuclear repeating units (Fig. 1a), in which each unit comprises two crystallographically distinct Cr ions bridged by a 1,2,3-triazolate ligand with Cr1–N1 and Cr2–N2 distances of 2.067(4) and 2.031(6) Å, respectively (Fig. 1b). In addition, the pores of the framework are occupied by disordered $CF_3SO_3^-$ ions. A careful analysis of the refined chemical occupancies reveals the presence of 0.34 $CF_3SO_3^-$ ions per Cr ion, which is close to the expected chemical formula of $Cr(tri)_2(CF_3SO_3)_{0.33}$ if each pore within the framework is filled with a single $CF_3SO_3^-$ ion. The presence of inserted $CF_3SO_3^-$ ions was further confirmed by the low Brunauer–Emmett–Teller surface area of 80 $m^2 g^{-1}$ calculated from a N_2 adsorption isotherm (Extended Data Fig. 2) and elemental analysis for C, H and N that is consistent with the formula $Cr(tri)_2(CF_3SO_3)_{0.33}$ (Methods). The presence of charge-balancing $CF_3SO_3^-$ ions in the pores of the framework indicates that the material contains mixed-valence $Cr^{II/III}$ centres (Supplementary Information).

A diffuse reflectance ultraviolet–visible–near-infrared spectrum of $Cr(tri)_2(CF_3SO_3)_{0.33}$ was obtained to confirm and further probe the mixed-valence electronic structure (Fig. 2a). Notably, the spectrum exhibits an intense absorption band in the near-infrared region between 5,000 and 12,000 cm^{-1}, with the absorbance increasing continuously to lower energies. We assigned the observed band to an intervalence charge-transfer transition between mixed-valence $Cr^{II/III}$ centres. Furthermore, the infrared spectrum of $Cr(tri)_2(CF_3SO_3)_{0.33}$ exhibits a broad absorption between 1,500 and 6,000 cm^{-1}, owing to extension of the intervalence charge-transfer transition band into the mid-infrared region (Fig. 2b). The absorption band masks most of the expected vibrational modes, to leave few detectable, sharp features. Indeed, absorption bands of similar energies are also reported for other mixed-valence coordination solids and charge transfer salts[21,24,28,29]. We note that the presence of such low-energy transitions suggests a negligible optical band gap that stems from a near-continuous distribution of mid-gap states.

Magnetic properties. Variable-temperature d.c. magnetic susceptibility measurements were performed to investigate the magnetic properties of $Cr(tri)_2(CF_3SO_3)_{0.33}$ (Fig. 3a). The plot of magnetization versus temperature features a gradual increase in magnetization on decreasing the temperature from 350 K, followed by a sudden increase below ~250 K. This sharp rise indicates a magnetic phase transition accompanied by an increased magnetic correlation length within the system. The plot exhibits the bifurcation of field-cooled and zero-field-cooled curves below the transition temperature, indicative of spontaneous magnetization. Furthermore, a Curie–Weiss fit to the inverse d.c. susceptibility data from 300 to 350 K affords $\theta_{CW} = 268$ K. The positive Curie-Weiss temperature suggests a dominant ferromagnetism, consistent with double exchange (Supplementary Information and Extended Data Fig. 3a). The presence of magnetic order was confirmed by a.c. magnetic susceptibility measurements (Extended Data Fig. 3b–f), which show sharp increases in both the in-phase (χ_M') and the out-of-phase (χ_M'') susceptibilities below 250 K. A precise magnetic ordering temperature was determined as $T_C = 225$ K by locating the temperature at which χ_M'' underwent a sharp increase from zero. To the best of our knowledge, $Cr(tri)_2(CF_3SO_3)_{0.33}$ exhibits the highest reported ferromagnetic ordering temperature among all coordination solids and the highest reported temperature for any type of magnetic order among structurally characterized metal–organic frameworks, with the previous records being $T_C = 107$ K for [{Ru_2(*m*-fluorobenzoate)$_4$}$_2$(BTDA-TCNQ)] (BTDA-TCNQ, bis(1,2,5-thiadiazolo)tetracyanoquinodimethane) and $T_N = 171$ K for $Mn(TCNE)_{3/2}(I_3)_{1/2}$ (TCNE, tetracyanoethylene), respectively[11,12,30,31]. The variable-field magnetization data collected between 3 and 270 K exhibit an S-shaped curve that quickly saturates at a magnetization of 2.39 μ_B mol^{-1} at 3 K, close to the expected value of 2.33 μ_B mol^{-1} for ferromagnetically coupled low-spin Cr^{II} and Cr^{III} centres present in a 2:1 ratio (Fig. 3c). We note that the presence of mixed-valence low-spin $Cr^{II/III}$ ions suggests that the itinerant electrons are housed in the t_{2g} orbitals. The magnetization data do not exhibit a notable hysteresis, with only a small remnant magnetization at all temperatures below T_C,

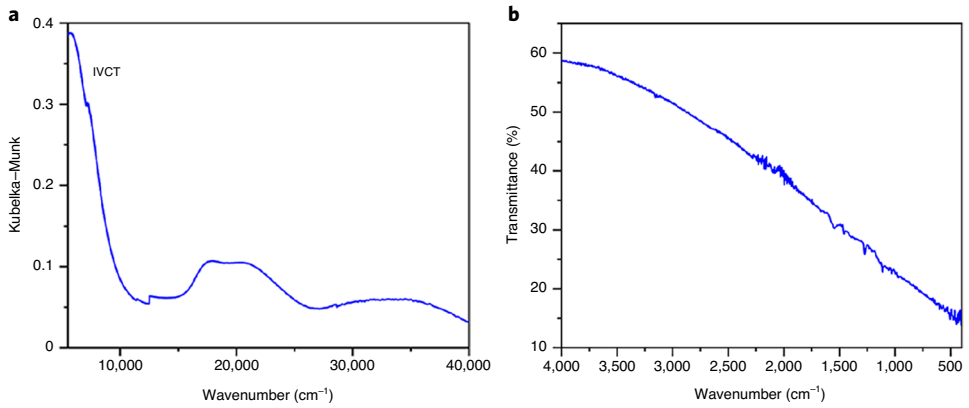

Fig. 2 | Spectroscopic characterization. a,**b**, Diffuse reflectance ultraviolet–visible–near-infrared (**a**) and infrared (**b**) spectra of $Cr(tri)_2(CF_3SO_3)_{0.33}$ collected at 300 K. The intense absorption band below 12,000 cm^{-1} that extends to the mid-infrared region is due to an intervalence charge-transfer transition from mixed-valence Cr ions.

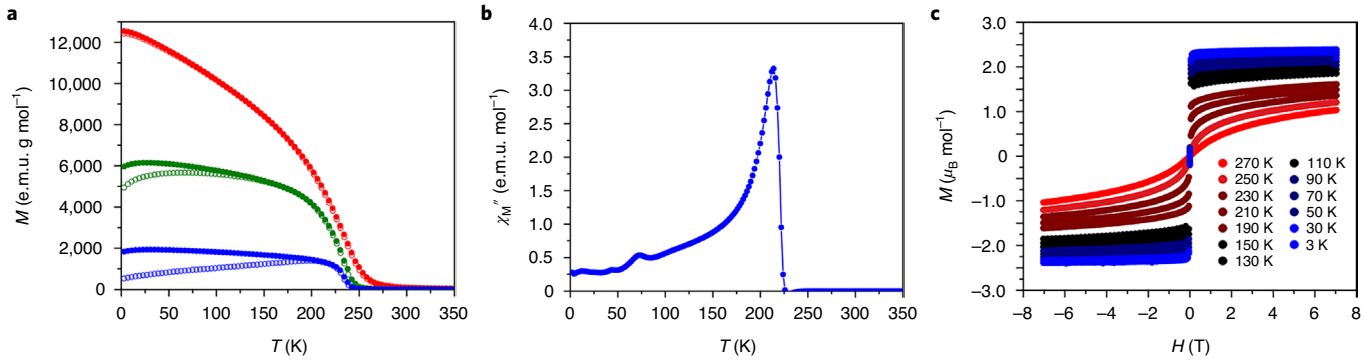

Fig. 3 | Magnetic properties of $Cr(tri)_2(CF_3SO3)_{0.33}$. a, Variable-temperature zero-field-cooled (open circles) and field-cooled (filled circles) magnetic susceptibility data collected at selected d.c. magnetic fields of 1,000 (red), 100 (green) and 25 Oe (blue). **b**, Variable-temperature out-of-phase a.c. magnetic susceptibility (χ_M'') collected with an a.c. oscillating magnetic field of 4 Oe at a frequency of 10 Hz and under a zero d.c. magnetic field. The sharp increase in χ_M'' suggests a magnetic ordering temperature of $T_C = 225$ K. **c**, Variable-field magnetization data collected at selected temperatures with a sweep rate of 33 Oe s^{-1}. The saturation magnetization value of 2.39 μ_B mol^{-1} at 3 K is consistent with ferromagnetically coupled mixed-valence low-spin $Cr^{II/III}$ ions.

which indicates that $Cr(tri)_2(CF_3SO_3)_{0.33}$ is a soft magnet. We note that the cubic crystal structure of the compound, which results in a clear lack of bulk magnetocrystalline anisotropy, is one of the dominant contributors to the observed magnetic behaviour with small hysteresis.

Electronic structure calculations. Insights into the electronic structure of $Cr(tri)_2(CF_3SO_3)_{0.33}$ were obtained using density functional theory (see Supplementary Information for the full computational details). Calculations were performed on the full three-dimensional unit cell, which contains 24 Cr atoms, 48 triazolate ligands and 8 triflate anions. The results suggest that the ferromagnetic state is lower in energy compared with that of the antiferromagnetic state by 0.127 eV per Cr atom, in agreement with the magnetic measurements. In the ferromagnetic state, the calculated saturation magnetic moment is 2.41 μ_B, which is in excellent agreement with the experimentally measured value of 2.39 μ_B. The band structure of $Cr(tri)_2(CF_3SO_3)_{0.33}$ (Fig. 4a) near the Fermi energy predominantly consists of spin-down bands with a large density of states and a band dispersion of ~1 eV, which suggests substantial spin polarization. Here, spin polarization is defined as the extent to which the spin is aligned in a particular direction[32]. The projected band structure (Fig. 4b) and projected density of states (Fig. 4d) show that both Cr *d* orbitals and N *p* orbitals of the triazolate ligands contribute to the valence band maximum and the conduction band minimum. Near the Fermi energy, the frontier orbitals of the bands are dominated by the Cr d_π orbitals and N *p* orbitals, with an approximately 32% hybridization between them, which indicates a strong hybridization between the Cr *d* and N *p* orbitals and π–*d* conjugation. Figure 4d also highlights spin polarization, as illustrated by the substantial peak in the spin-down density at the Fermi energy for both the total and the Cr *d* orbitals. This shows that the Cr *d* orbitals primarily contribute to the spin-polarized state. The localized charge density (Extended Data Fig. 4) shows alternating high and low charge Cr centres. The Cr centres of lower and higher charges exhibit lower and higher magnetic moments, respectively, consistent with the mixed-valence low-spin $Cr^{II/III}$ centres. Notably, the charge density and projected density of states both indicate spin polarization. Taken together, these computational results demonstrate a ferromagnetic ground state for $Cr(tri)_2(CF_3SO_3)_{0.33}$, and the high density of spin-polarized bands near the Fermi energy that arises from a strong π–*d* hybridization suggests the delocalization of electrons in the valence band maximum, consistent with a double exchange that stems from the mixed-valence metal centres.

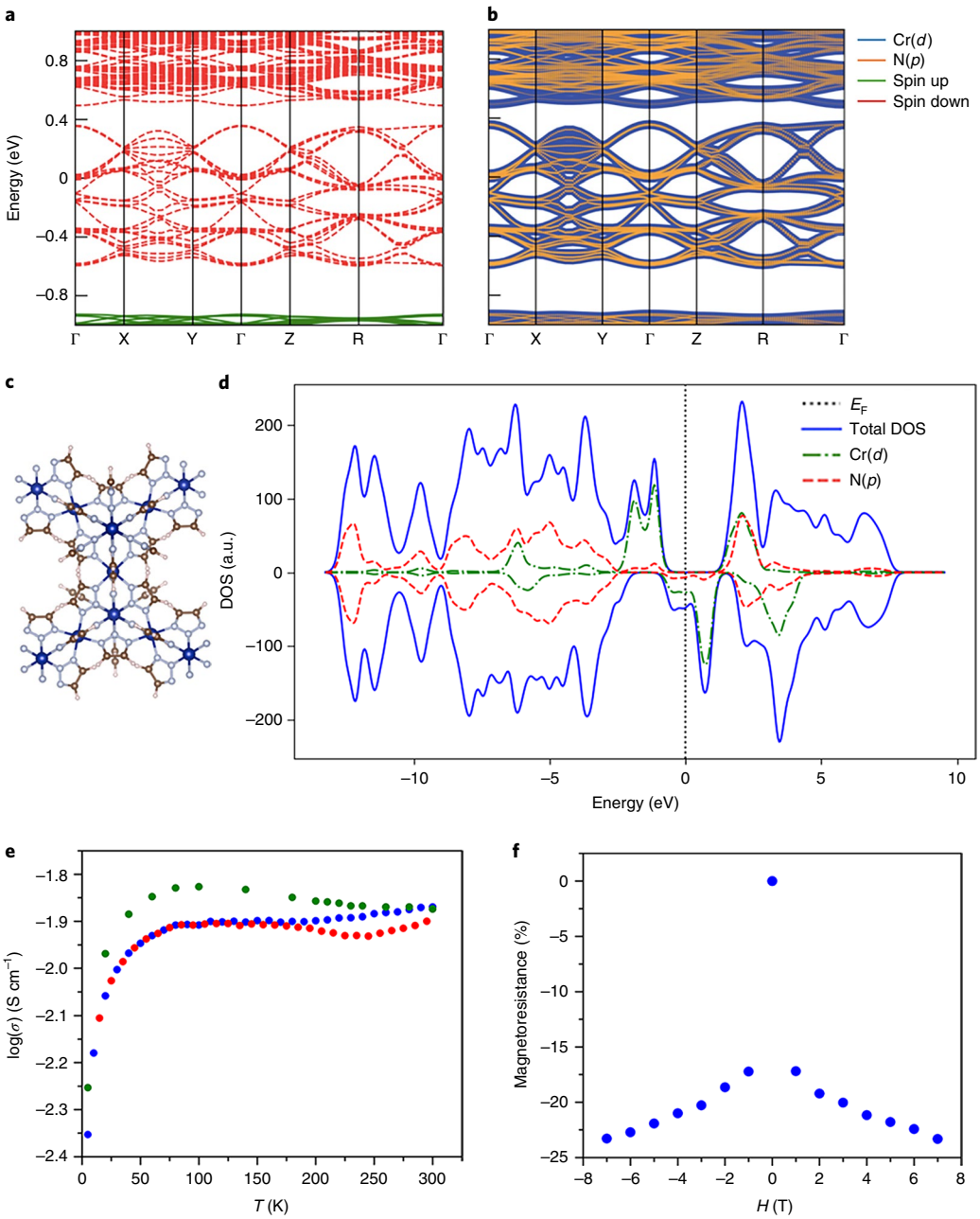

Fig. 4 | Electronic structure calculations and electronic conductivity of $Cr(tri)_2(CF_3SO_3)_{0.33}$. a,b, Total (**a**) and projected (**b**) band structure for the ferromagnetic state, calculated using the Perdew–Burke–Ernzerhof functional. The zero energy is set to the highest occupied state. The symmetry points correspond to Γ = (0,0,0), X = (0.5,0,0), Y = (0,0.5,0), Z = (0,0,0.5) and R = (0.5,0.5,0.5). The dense spin-down bands near the Fermi energy (E_F) have dominant contributions from the strongly hybridized Cr d_π and N *p* orbitals. **c**, The geometry-optimized structure of $Cr(tri)_2(CF_3SO_3)_{0.33}$. Cr, blue; N, light blue; C, brown; O, white; the $CF_3SO_3^-$ ion is omitted for clarity. **d**, Partial density of states (DOS) for the ferromagnetic state. Zero energy is set to the highest occupied state, denoted by the dotted vertical line. **e**, Variable-temperature conductivity data of $Cr(tri)_2(CF_3SO_3)_{0.33}$. Blue and red spheres represent measurements taken during cooling and warming, respectively. Green spheres represent data collected while cooling under an applied magnetic field of 7 T. The increased conductivity under a magnetic field below T_C is consistent with a negative magnetoresistance. **f**, Magnetoresistance data of $Cr(tri)_2(CF_3SO_3)_{0.33}$ collected at 5 K under selected d.c. magnetic fields with a maximum negative magnetoresistance of ~23% at 7 T. a.u., arbitrary units.

Electronic conductivity and magnetoresistance. Variable-temperature conductivity measurements were performed to investigate the charge-transport properties associated with the double exchange in $Cr(tri)_2(CF_3SO_3)_{0.33}$ (Fig. 4e and Extended Data Fig. 5). On cooling from 300 to 200 K, the conductivity decreased very slightly from $\sigma = 1.4(1) \times 10^{-2}$ to $1.3(1) \times 10^{-2}$ S cm^{-1}. Despite the presence of a slight hysteresis between the data measured on cooling and that on warming of the sample, the cooling data above 200 K could be fit using the three-dimensional variable-range hopping model (Supplementary Information). Below T_C and down to 80 K, the compound exhibited a conductivity that is nearly temperature independent, with $\sigma \approx 1.2(1) \times 10^{-2}$ S cm^{-1}. An Arrhenius fit to the data in this temperature range yielded a small activation energy of 0.14 meV, suggestive of highly delocalized charge carriers. On cooling below 80 K, we observed a decrease in conductivity to $\sigma = 4.4(1) \times 10^{-3}$ S cm^{-1} at 5 K. The low-temperature data are best fit with the Efros–Shklovskii

variable-range hopping model, which highlights a transition back to localized small polarons (Supplementary Information)[33]. Next, conductivity measurements were performed on the same sample pellet while cooling the cell under an applied field of 7 T. Strikingly, the conductivity increased as the temperature was lowered from 225 to 80 K. At 5 K, $Cr(tri)_2(CF_3SO_3)_{0.33}$ exhibited a maximum negative magnetoresistance of ~23% (Fig. 4f), which represents one of the highest values for any coordination solid[34–37] .The observed barrierless transport behaviour in conjunction with the large negative magnetoresistance is consistent with a double-exchange mechanism in $Cr(tri)_2(CF_3SO_3)_{0.33}$. The computational results suggest that the partially filled spin-down bands near the Fermi level give rise to a current density that is carried mainly by spin-down charge carriers. Owing to the spin-polarized current, the presence of any tunnelling junctions that consist of ferromagnetic domains/layers can yield large magnetoresistance. As $Cr(tri)_2(CF_3SO_3)_{0.33}$ is a soft ferromagnet, the material most likely consists of randomly aligned ferromagnetic domains under a zero applied magnetic field. Under an applied magnetic field, the ferromagnetic domains can align parallel to each other, which allows a facile transport of spin-polarized currents. Indeed, large negative magnetoresistance has commonly been observed in solid-state materials with itinerant ferromagnetism[38,39].

Conclusions

The foregoing results demonstrate the observation of itinerant ferromagnetism in a metal–organic framework, which gives rise to a magnetic ordering temperature of $T_C = 225$ K and a large negative magnetoresistance. Additionally, this synthetic approach of using π–d conjugation between organic linkers and mixed-valence metal centres with diffuse d_π orbitals provides a general blueprint from which to design materials with improved magnetic and charge-transport properties, given the vast chemical versatility offered by metal–organic frameworks.

Online content

Any methods, additional references, Nature Research reporting summaries, source data, extended data, supplementary information, acknowledgements, peer review information; details of author contributions and competing interests; and statements of data and code availability are available at https://doi.org/10.1038/s41557-021-00666-6.

Received: 26 May 2020; Accepted: 18 February 2021;
Published online: 15 April 2021

References

1. Gutfleicsch, O. et al. Magnetic materials and devices for the 21st century: stronger, lighter and more energy efficient. *Adv. Mater.* **23**, 821–842 (2011).
2. Felser, C., Fecher, G. H. & Balke, B. Spintronics: a challenge for materials science and solid-state chemistry. *Angew. Chem. Int. Ed.* **46**, 668–699 (2007).
3. Coronado, E., Palacio, F. & Veciana, J. Molecule-based magnetic materials. *Angew. Chem. Int. Ed.* **42**, 2570–2572 (2003).
4. Kübler, J. *Theory of Itinerant Electron Magnetism* (Oxford Univ. Press, 2000).
5. Zener, C. Interaction between the *d*-shells in the transition metals. II. Ferromagnetic compounds of manganese with perovskite structure. *Phys. Rev.* **82**, 403–405 (1951).
6. Briceño, G., Chang, H., Sun, X., Schultz, P. G. & Xiang, X.-D. A class of cobalt oxide magnetoresistance materials discovered with combinatorial synthesis. *Science* **270**, 273–275 (1995).
7. Şaşıoğlu, E., Sandratskii, L. M. & Bruno, P. Role of conduction electrons in mediating exchange interactions in Mn-based Heusler alloys. *Phys. Rev. B* **77**, 064417 (2008).
8. Yaghi, O. M. et al. Reticular synthesis and the design of new materials. *Nature* **423**, 705–714 (2003).
9. Calbo, J., Golomb, M. J. & Walsh, A. Redox-active metalo-organic frameworks for energy conversion and storage. *J. Mater. Chem. A* **7**, 16571–16597 (2019).
10. Yin, Z., Wan, S., Yang, J., Kurmoo, M. & Zeng, M.-H. Recent advances in post-synthetic modification of metal–organic frameworks: new types and tandem reactions. *Coord. Chem. Rev.* **378**, 500–512 (2019).
11. Dechambenoit, P. & Long, J. R. Microporous magnets. *Chem. Soc. Rev.* **40**, 3249–3265 (2011).
12. Thorarinsdottir, A. E. & Harris, T. D. Metal–organic framework magnets. *Chem. Rev.* **120**, 8716–8789 (2020).
13. Kosaka, W. et al. Gas-responsive porous magnet distinguishes the electron spin of molecular oxygen. *Nat. Commun.* **9**, 5420 (2018).
14. Ruiz, E., Rodríguez-Fortea, A., Alvarez, S. & Verdaguer, M. Is it possible to get high T_C magnets with Prussian blue analogues? A theoretical prospect. *Chem. Eur. J.* **11**, 2135–2144 (2005).
15. Mallah, T., Thiébaut, S., Verdaguer, M. & Veillet, P. High-T_C molecular-based magnets: ferrimagnetic mixed-valence chromium(III)–chromium(II) cyanide with T_C at 240 and 190 Kelvin. *Science* **262**, 1554–1557 (1993).
16. Ferlay, S., Mallah, T., Ouahès, R., Veillet, P. & Verdaguer, M. A room-temperature organometallic magnet based on Prussian blue. *Nature* **378**, 701–703 (1995).
17. Holmes, S. M. & Girolami, G. S. Sol–gel synthesis of $KV^{II}[Cr^{III}(CN)_6]\cdot 2H_2O$: a crystalline molecule-based magnet with a magnetic ordering above 100 °C. *J. Am. Chem. Soc.* **121**, 5593–5594 (1999).
18. Manriquez, J. M., Yee, G. T., McLean, R. S., Epstein, A. J. & Miller, J. S. A room-temperature molecular/organic-based magnet. *Science* **252**, 1415–1417 (1991).
19. Bechlar, B. et al. High-spin ground states via electron delocalization in mixed-valence imidazolate-bridged divanadium complexes. *Nat. Chem.* **2**, 362–368 (2010).
20. Gaudette, A. I. et al. Electron hopping through double-exchange coupling in a mixed-valence diiminobenzoquinone-bridged Fe_2 complex. *J. Am. Chem. Soc.* **137**, 12617–12626 (2015).
21. Schulze, B. & Schubert, U. S. Beyond click chemistry—supramolecular interactions of 1,2,3-triazoles. *Chem. Soc. Rev.* **43**, 2522–2571 (2014).
22. Aubrey, M. L. et al. Electron delocalization and charge mobility as a function of reduction in a metal–organic framework. *Nat. Mater.* **17**, 625–632 (2018).
23. Zhang, J. P., Zhang, Y. B., Lin, J. B. & Chen, X. M. Metal azolate frameworks: from crystal engineering to functional materials. *Chem. Rev.* **112**, 1001–1033 (2012).
24. Park, J. G. et al. Charge delocalization and bulk electronic conductivity in the mixed-valence metal–organic framework $Fe(1,2,3\text{-triazolate})_2(BF_4)_x$. *J. Am. Chem. Soc.* **140**, 8526–8534 (2018).
25. Brunschwig, B. S., Creutz, C. & Sutin, N. Optical transitions of symmetrical mixed-valence systems in the class II–III transition regime. *Chem. Soc. Rev.* **31**, 168–184 (2002).
26. Gándara, F. et al. Porous, conductive metal–triazolates and their structural elucidation by the charge-flipping method. *Chem. Eur. J.* **18**, 10595–10601 (2012).
27. Zhou, X.-H., Peng, Y.-H., Du, X.-D., Zuo, J.-L. & You, X.-Z. Hydrothermal syntheses and structures of three novel coordination polymers assembled from 1,2,3-triazolate ligands. *Cryst. Eng. Comm.* **11**, 1964–1970 (2009).
28. Collman, J. P. et al. Synthetic, electrochemical, optical, and conductivity studies of coordination polymers of iron, ruthenium, and osmium octaethylporphyrin. *J. Am. Chem. Soc.* **109**, 4606–4614 (1987).
29. Tanner, D. B., Jacobsen, C. S., Garito, A. F. & Heeger, A. J. Infrared studies of the energy gap in tetrathiofulvalene-tetracyanoquinodimethane (TTF-TCNQ). *Phys. Rev. B* **13**, 3381–3404 (1976).
30. Motokawa, N., Miyasaka, H., Yamashita, M. & Dunbar, K. R. An electron-transfer ferromagnet with $T_C = 107$ K based on a three-dimensional $[Ru_2]_2$/TCNQ system. *Angew. Chem. Int. Ed.* **47**, 7760–7763 (2008).
31. Stone, K. H. et al. $Mn^{II}(TCNE)_{3/2}(I_3)_{1/2}$—a 3D network-structured organic-based magnet and comparison to a 2D analog. *Adv. Mater.* **22**, 2514–2519 (2010).
32. Kessler, J. *Polarized Electrons* (Springer, 1985).
33. Efros, A. L. & Shklovskii, B. I. Coulomb gap and low temperature conductivity of disordered systems. *J. Phys. C* **8**, L49–L56 (1975).
34. Raju, N. P. et al. Anomalous magnetoresistance in high-temperature organic-based magnetic semiconducting $V(TCNE)_x$ films. *J. Appl. Phys.* **93**, 6799 (2003).
35. Coronado, E., Prieto-Ruiz, J. P. & Prima-Garcia, H. Spin polarization in electrodeposited thin films of the molecule-based magnetic semiconductor $Cr_{5.5}(CN)_{12}\cdot 11.5H_2O$. *Chem. Commun.* **49**, 10145–10147 (2013).
36. Lu, Y. et al. Thin-film deposition of an organic magnet based on vanadium methyl tricyanoethylenecarboxylate. *Adv. Mater.* **26**, 7632–7636 (2014).
37. Black, N. et al. Giant negative magnetoresistance in Ni(quinoline-8-selenoate)$_2$. *Phys. Chem. Chem. Phys.* **20**, 514–519 (2018).
38. Coey, J. M. D. & Venkatesan, M. Half-metallic ferromagnetism: example of CrO_2. *J. Appl. Phys.* **91**, 8345–8350 (2002).
39. Xiao, J. Q., Jian, J. S. & Chien, C. L. Giant magnetoresistance in nonmultilayer magnetic systems. *Phys. Rev. Lett.* **68**, 3749–3752 (1992).

Methods

Synthesis of Cr(tri)$_2$(CF$_3$SO$_3$)$_{0.33}$. All the handling of Cr(tri)$_2$(CF$_3$SO$_3$)$_{0.33}$ was performed under a dry N_2 or Ar atmosphere. Liquid 1*H*-1,2,3-triazole (1.04 g, 15.0 mmol) was added to a 20 ml glass scintillation vial that contained a solution of Cr(CF$_3$SO$_3$)$_2$ (1.75 g, 5.00 mmol) in 10 ml of dimethylformamide. The vial was sealed with a polytetrafluoroethylene-lined cap and heated at 120 °C for three days. The resulting suspension was cooled to 25 °C and filtered with a Nylon membrane filter to yield a dark purple powder. The powder was washed by soaking in dimethylformamide (3 × 15 ml) and then in dichloromethane (4 × 15 ml), and was then dried under a dynamic vacuum (<10 μbar) at 130 °C for 48 h to afford 0.356 g (30%) of the product as a purple microcrystalline powder. Anal. Calculated for $CrC_{4.33}H_4N_6FS_{0.33}O$: C, 21.91; H, 1.70; N, 35.41. Found: C, 22.24; H, 1.44; N, 35.21.

Magnetic measurements. In a glove box under a N_2 atmosphere, a sample was prepared by adding an activated powder into a 5-mm-inner-diameter quartz tube that contained a raised quartz platform. The sample powder was restrained with a plug of compacted glass wool to prevent crystallite torqueing during the measurements. The quartz tube was transferred to a Schlenk line and evacuated until the internal pressure reached 30 mtorr. The tube was cooled in liquid N_2 and flame sealed under a static vacuum. All the magnetic measurements were performed using a Quantum Design MPMS2 SQUID magnetometer from 3 to 350 K at applied magnetic fields that ranged from 0 to ±7 T. The a.c. susceptibility measurements were performed with an oscillating field of 4 Oe with a frequency from 1 to 100 Hz. Diamagnetic corrections were applied to the data using Pascal's constants to give $\chi_D = -0.00009744$ e.m.u. mol^{-1}.

Electrical conductivity measurements. Conductivity measurements were performed using a homebuilt four-contact cell (Supplementary Fig. 5a). In a glove box under an Ar atmosphere, a sample pellet was manually pressed in a cell with a known inner cell diameter. While pressed, the cell was sealed with Torr Seal low-vapour-pressure epoxy. When the epoxy dried completely, the cell was removed from the press for the sample pellet thickness to be measured using a caliper. Room-temperature conductivity measurements were performed using a Bio-Logic VMP-3 multipotentiostat fitted to the Ar glove box. Variable-temperature conductivity measurements were performed in a Quantum Design MPMS2 SQUID magnetometer with a modified sample rod that accommodated ten 26 AWG silver-coated copper cables sealed at the top of the rod with an air-tight Swagelock fitting and Torr Seal low-vapour-pressure epoxy. The airtight sample cell was attached to the SQUID sample rod and inserted into the cryostat-equipped SQUID chamber at 300 K. Current–voltage profiles between 5 and 300 K were collected with a Bio-Logic SP200 potentiostat by scanning the current between ±50 μA and the sample cell allowed to equilibrate for at least 30 min between each measured temperature. All the data collected were ohmic within a ±50 μA window and were then modelled with Ohm's law, $E \times \sigma = j$, where E is the applied electric field and j is the current density, to determine the sample conductivity with σ in the units S cm^{-1}. Magnetoresistance measurements were performed by applying magnetic fields that ranged from 0 to ±7 T during the current–voltage profile collections. Data were fitted to charge-transport models as described in the Supplementary Information.

High-resolution powder X-ray diffraction. The powder sample was packed into a 1.0 mm boron-rich glass capillary tube inside a glove box under a N_2 atmosphere. The capillary was flame sealed and placed inside a Kapton tube that was sealed at both ends with epoxy. High-resolution synchrotron X-ray powder diffraction data were collected at Beamline 11-BM at the Advanced Photon Source (APS) at Argonne National Laboratory. Diffraction patterns were collected at 360, 220 and 120 K with a wavelength of 0.412685 Å. Discrete detectors that covered an angular range from −6 to 16° in 2θ were scanned over a 34° range of 2θ, with data points collected every 0.001° in 2θ and at a scan speed of 0.01° s^{-1}. For all the diffraction data from Beamline 11-BM, precise unit-cell dimensions were determined by performing Pawley refinements, after which Rietveld refinements were performed using the software package TOPAS-Academic[40]. High-resolution synchrotron X-ray powder diffraction data between 270 and 5 K (Supplementary Fig. 7a) were collected at Beamline BM31 at the European Synchrotron Radiation Facility (ESRF) with a wavelength of 0.49754758 Å.

Powder neutron diffraction. Powder neutron diffraction data were collected on the POWGEN instrument at the Spallation Neutron Source at Oak Ridge National Laboratory. Approximately 1 g of sample was loaded into a vanadium POWGEN Automatic Changer can in an He-filled glove box. Data were collected at the selected temperatures of 300, 150 and 10 K in the high-resolution mode[41].

Data availability

All data supporting the findings of this study are available within the paper and its Supplementary Information files. Source data are provided with this paper.

References

40. Coelho, A. A. TOPAS-Academic v. 5 (Coelho Software, 2017).
41. Huq, A. et al. POWGEN: rebuild of a third-generation powder diffractometer at the Spallation Neutron Source. *J. Appl. Cryst.* **52**, 1199–1201 (2019).

Acknowledgements

This research was supported by the National Science Foundation (NSF) Award no. DMR-1611525, with the exception of the measurement and analysis of the magnetic data, which were supported by the Nanoporous Materials Genome Center of the US Department of Energy, Office of Basic Energy Sciences, Division of Chemical Sciences, Geosciences and Biosciences under Award no. DE-FG02-17ER16362. Powder X-ray diffraction data were collected at Beamline 11-BM at the APS, operated by Argonne National Laboratory, and beamline BM31 at the ESRF. We are grateful to our local contact at the ESRF for providing assistance in using beamline BM31. Use of the APS at Argonne National Laboratory was supported by US Department of Energy, Office of Science, Office of Basic Energy Sciences, under Contract no. DE-AC02-06CH11357. Data from Beamline 11-BM were collected as part of the 2018 Modern Methods in Rietveld Refinement and Structural Analysis workshop, a school supported by the US National Committee for Crystallography and the American Crystallographic Association. Neutron diffraction data were collected at the POWGEN beamline at the Spallation Neutron Source, a DOE Office of Science User Facility operated by the Oak Ridge National Laboratory. Soft X-ray absorption spectroscopy data were collected at Beamline 8.0.1 at the Advanced Light Source of Lawrence Berkeley National Laboratory, a Department of Energy Office of Science User Facility under Contract no. DE-AC02-05CH11231. Electronic structure calculations utilized an award of computer time provided by the ASCR Leadership Computing Challenge (ALCC) program and resources of the National Energy Research Scientific Computing Center, a US Department of Energy Office of Science User Facility operated under Contract no. DE-AC02-05CH11231. Additional computation resources were provided by the Minnesota Supercomputing Institute at the University of Minnesota. T.R. thanks the Welch Foundation (Grant no. N-2012-20190330) for funding. In addition, we thank J. Oktawiec, S. H. Lapidus, X. Wenqian, P. Khalifah, Q. Zhang, M. J. Kirkham, Y.-S. Liu and G. Ren for discussions and experimental assistance, and T.D.H. for editorial assistance. We also thank the National Science Foundation and National GEM Consortium for providing graduate fellowship supports for J.G.P. and B.A.C., respectively.

Author contributions

J.G.P. and J.R.L. formulated the project. J.G.P. synthesized the compound. B.A.C. and J.D.G. performed electronic structure calculations and analysed the data. J.G.P. and L.E.D. collected and analysed the magnetic data. M.E.Z. collected X-ray absorption spectroscopy data. J.G.P. and M.L.A. collected and analysed conductivity data. E.V. collected scanning electron microscopy images. H.Z.H.J. collected and analysed the infrared spectra. J.G.P. collected and analysed powder X-ray diffraction data from the APS, with assistance from T.R. M.A.G. collected and analysed powder X-ray diffraction data from the ESRF. M.A.G. and J.G.P. collected and analysed powder neutron diffraction data. J.G.P. and J.R.L. wrote the paper, and all the authors contributed to revising it.

Competing interests

The authors declare no competing interests.

Additional information

Extended data is available for this paper at https://doi.org/10.1038/s41557-021-00666-6.

Supplementary information The online version contains supplementary material available at https://doi.org/10.1038/s41557-021-00666-6.

Correspondence and requests for materials should be addressed to J.R.L.

Peer review information *Nature Chemistry* thanks Talal Mallah and the other, anonymous, reviewer(s) for their contribution to the peer review of this work.

Reprints and permissions information is available at www.nature.com/reprints.

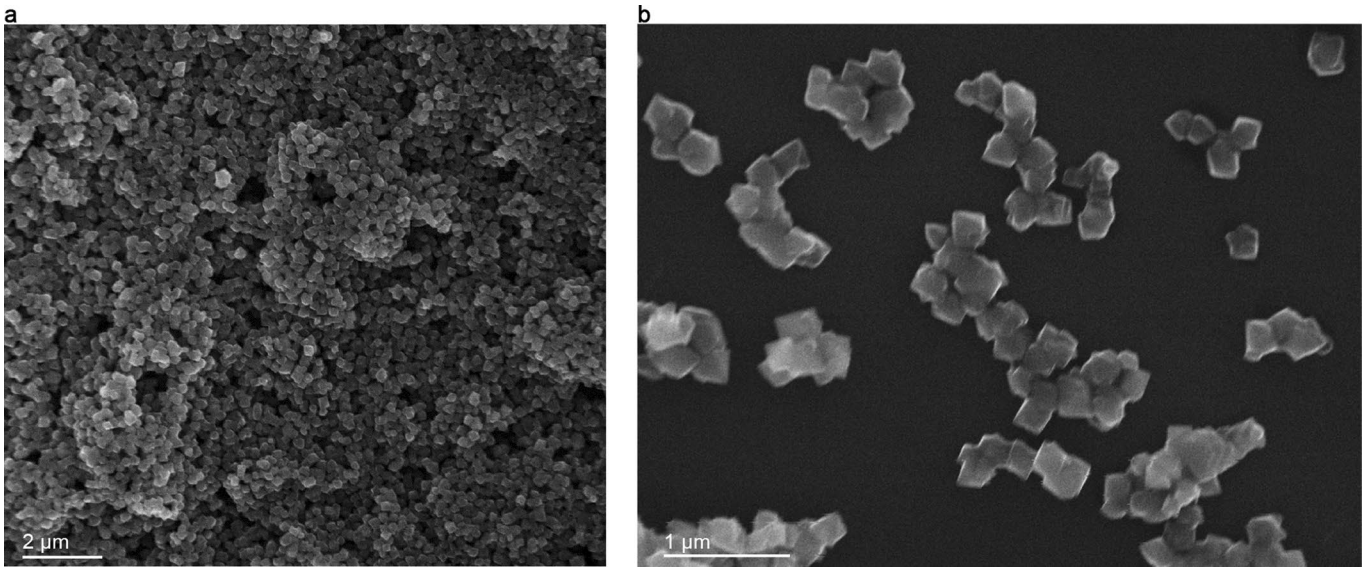

Extended Data Fig. 1 | Scanning electron microscopy images of $Cr(tri)_2(CF_3SO_3)_{0.33}$ crystals. a,b Scanning electron microscopy images of microcrystalline $Cr(tri)_2(CF_3SO_3)_{0.33}$ powder. Octahedron-shaped crystals have an average edge dimension of ~0.5 µm. Scale bars 2 µm **(a)** and 1 µm **(b)**.

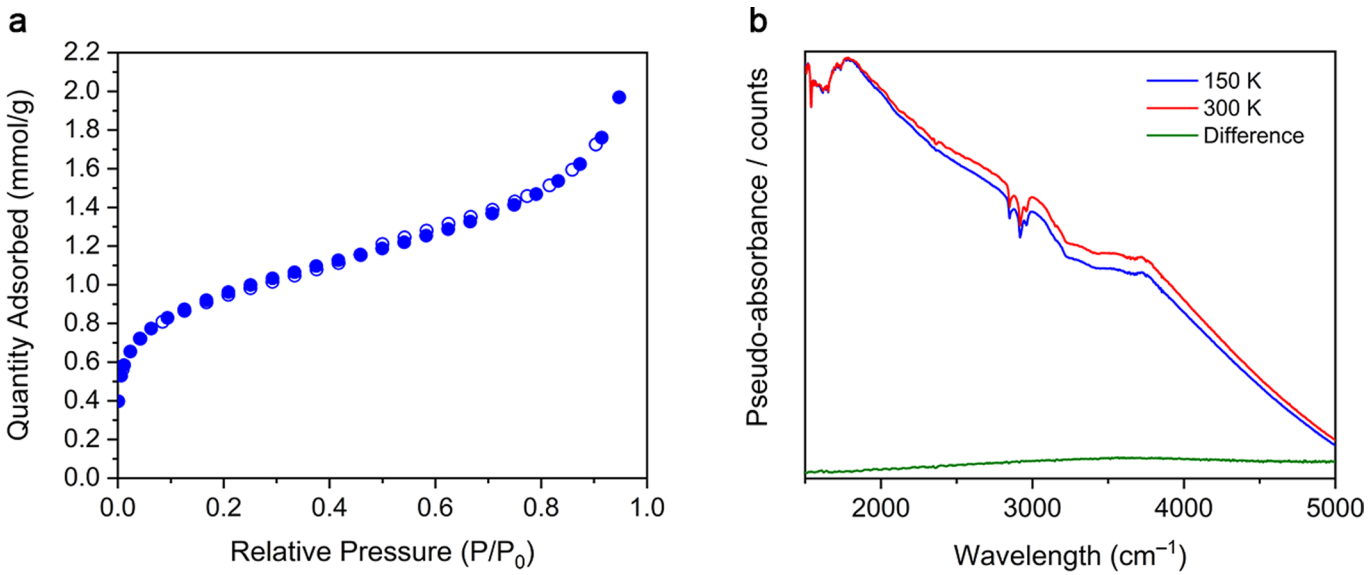

Extended Data Fig. 2 | Analyses of the Cr mixed-valency. a, N2 adsorption isotherm collected at 77 K for $Cr(tri)_2(CF_3SO_3)_{0.33}$. Closed and open data points represent adsorption and desorption, respectively. **b**, Infrared data collected at 150 K (blue) and 300 K (red) and the difference plot (green) for $Cr(tri)_2(CF_3SO_3)_{0.33}$.

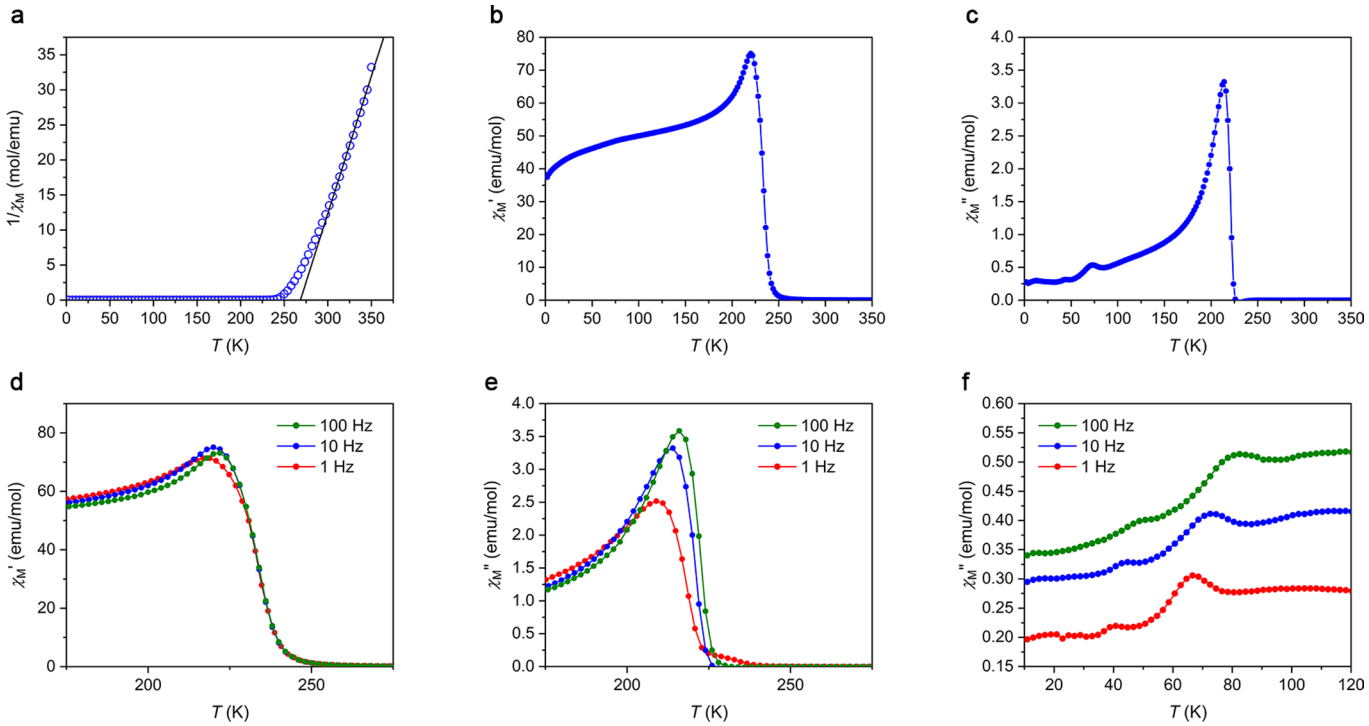

Extended Data Fig. 3 | Magnetic data. a, Variable-temperature magnetic susceptibility data (χ_M) for $Cr(tri)_2(CF_3SO_3)_{0.33}$ collected under the applied dc field of 25 Oe. Data plotted as $1/\chi_M$ versus temperature. Curie-Weiss fit to the data between 300 K and 350 K is shown by a black solid line, with fitting parameters described in the main text. **b-f**, Variable-temperature in-phase (χ') and out-of-phase (χ'') ac magnetic susceptibility of $Cr(tri)_2(CF_3SO_3)_{0.33}$ at selected frequencies of 4 Oe ac oscillating magnetic field and zero dc magnetic field.

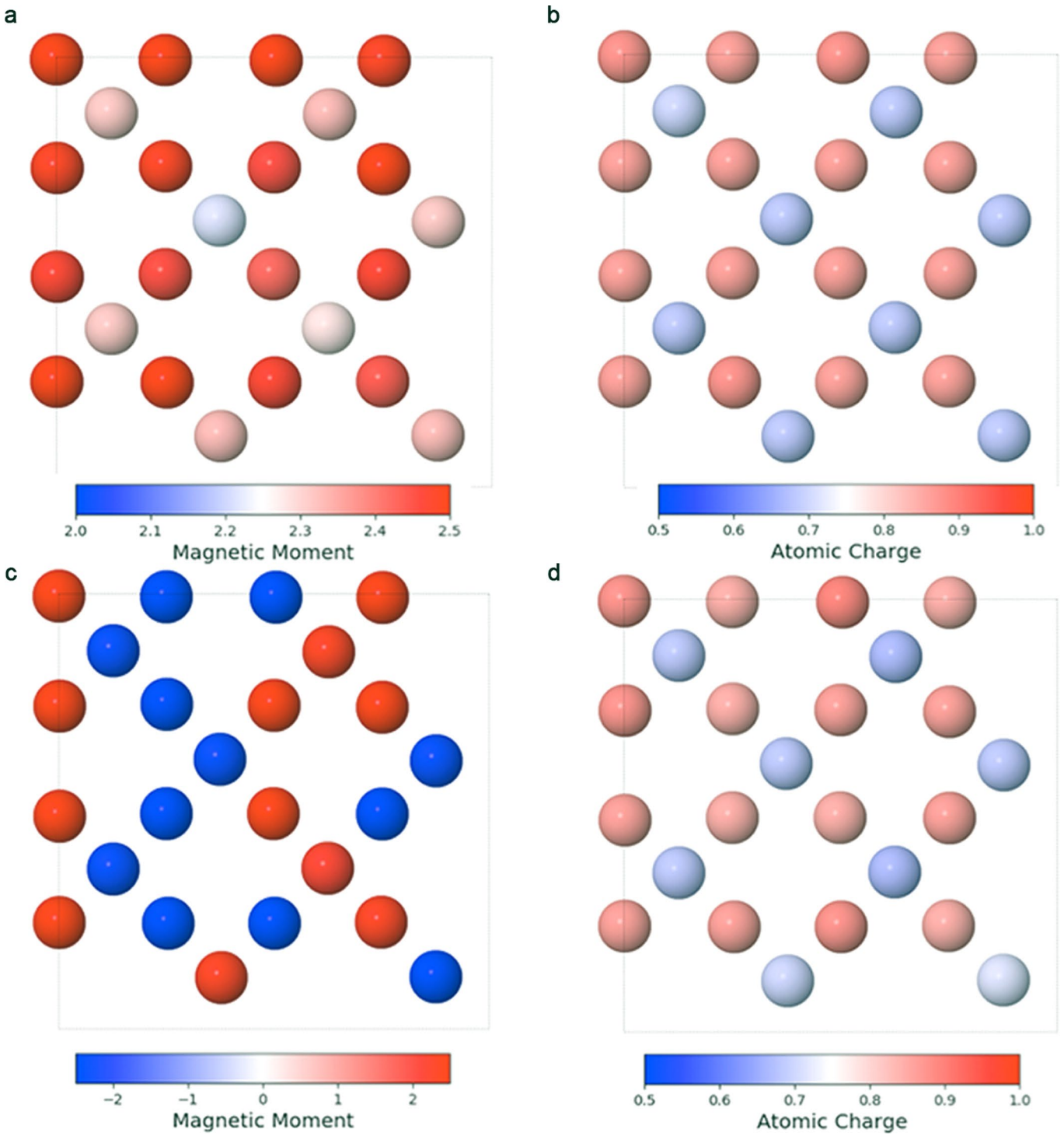

Extended Data Fig. 4 | Charge analysis. a, Magnetic moments (μ_B mol^{-1}) for the ferromagnetic state. **b**, Atomic charge for the ferromagnetic state in atomic units. **c**, Magnetic moments (μ_B mol^{-1}) for the antiferromagnetic state. **d**, Atomic charge for the antiferromagnetic state in atomic units. Atomic properties shown as a gradient from blue to white to red. Negative magnetic moments indicate spin-down contributions.

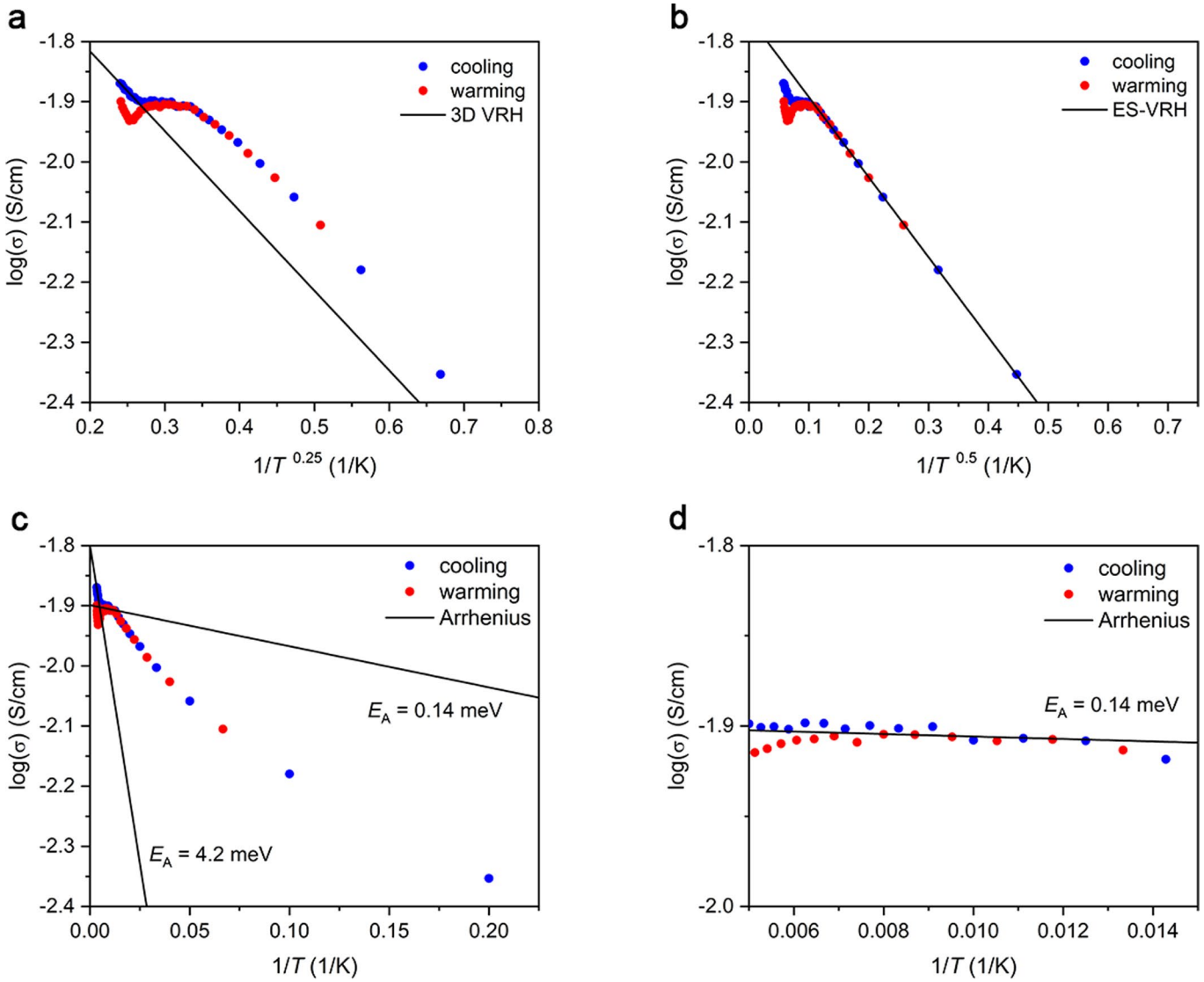

Extended Data Fig. 5 | Variable temperature conductivity data modeling. a-d, Variable-temperature log(σ) data of $Cr(tri)_2(CF_3SO_3)_{0.33}$ plotted versus $1/T^{0.25}$ (**a**), $1/T^{0.5}$ (**b**), and $1/T$ and fitted with three-dimensional variable-range hopping, Efros-Shklovskii variable-range hopping, and Arrhenius models, respectively (**c**, **d**). For clarity, log(σ) versus $1/T$ plot (**c**) has been zoomed-in to the intermediate temperature region (**d**) where conductivity exhibits a weak temperature dependence.